Tunable polymorphism of epitaxial iron oxides in the four-in-one ferroic-on-GaN system with magnetically ordered α-, γ-, ε-Fe_2O_3, and Fe_3O_4 layers

S. M. Suturin,[1,*] A. M. Korovin,[1] S. V. Gastev,[1] M. P. Volkov,[1] A. A. Sitnikova,[1] D. A. Kirilenko,[1]
M. Tabuchi,[2] and N. S. Sokolov[1]
[1]*Ioffe Institute, 26 Polytechnicheskaya street, St. Petersburg 194021, Russia*
[2]*Synchrotron Radiation Research Center, Nagoya University, Furo-cho, Chikusa, Nagoya 464-8603, Japan*

(Received 12 August 2017; revised manuscript received 29 May 2018; published 23 July 2018)

Hybridization of semiconducting and magnetic materials into a single heterostructure is believed to be potentially applicable to the design of functional spintronic devices. In the present work we report epitaxial stabilization of four magnetically ordered iron oxide phases (Fe_3O_4, γ-Fe_2O_3, α-Fe_2O_3 and most exotic metastable ε-Fe_2O_3) in the form of nanometer-sized single crystalline films on GaN(0001) surface. The epitaxial growth of four distinctly different iron oxide phases is achieved by a single-target pulsed laser deposition technology on a GaN semiconductor substrate widely used for electronic device fabrication. The discussed iron oxides belong to a family of simple formula magnetic materials exhibiting a rich variety of outstanding magnetic properties including peculiar Verwey and Morin phase transitions in Fe_3O_4 and α-Fe_2O_3 and multiferroic behavior in metastable magnetically hard ε-Fe_2O_3 ferrite. The physical reasons standing behind the nucleation of a particular phase in an epitaxial growth process is discussed in the present paper deserving interest from the fundamental point of view. The practical side of the presented study is to exploit the tunable polymorphism of iron oxides in order to create the ferroic-on-semiconductor heterostructures usable in spintronic devices. By application of a wide range of experimental techniques the surface morphology, crystalline structure and electronic and magnetic properties of the single phase iron oxide epitaxial films on GaN have been studied. A comprehensive comparison has been made to the properties of the same ferrite materials in the bulk and nanostructured form reported by other research groups.

DOI: 10.1103/PhysRevMaterials.2.073403

I. INTRODUCTION

Hybrid heterostructures combining closely spaced semiconducting and magnetic layers are believed to be promising candidates to be used in functional spintronic devices. Unlike diluted magnetic semiconductors, the hybrid heterostructures allow separate control over the magnetic and electrical properties. The magnetic layers in such heterostructures must preferably be dielectric or have controllable conductivity as the high concentration of the free charge carriers at the interface would provide an additional nonradiative recombination channel leading to a significant deterioration of the semiconducting properties. Transparency of the magnetic layer in the visible range would be a favorable property as long as the optoelectronic features of the semiconducting device are to be exploited. Making choice of the magnetic material for the hybrid heterostructure, one could consider iron oxides as the suitable candidates. Including FeO, Fe_3O_4, and a number of Fe_2O_3 polymorphs (α-Fe_2O_3, β-Fe_2O_3, γ-Fe_2O_3, and ε-Fe_2O_3), the iron oxides constitute a big family of magnetic materials exhibiting a rich variety of outstanding physical properties and presenting interest for both technological applications and fundamental studies. The different iron oxide polymorphs have drastically different crystal structure and consequently exhibit a variety of magnetic properties. The comprehensive description of the bulk lattice structure and magnetic characteristics of α-Fe_2O_3 (hematite), Fe_3O_4 (magnetite), γ-Fe_2O_3 (maghemite), and ε-Fe_2O_3 is given in the supplemental materials section of this paper [1]. Due to numerous applications, the fabrication of various iron oxides in nanoscale form has been widely studied during the past decades. Growth of iron ferrite nanoparticles has been performed by a variety of methods [2]. Epitaxial layers have been grown on different substrates (InAs, GaAs, $MgAl_2O_4$, Si, etc.) using reactive oxygen or ozone assisted molecular beam epitaxy, reactive magnetron sputtering, and pulsed laser deposition. Surprisingly there exist very few works describing hybridization of the iron oxides with GaN, the semiconductor widely used in the modern high-power electronics. It is believed that the controllable spontaneous magnetization/polarization of the iron oxides may add new functionality to the GaN-based semiconductor devices, e.g., can be used for impedance matching spin injection [3] or for ferroelectric gate insulators. Of various iron oxides only Fe_3O_4 has ever been grown on GaN by annealing a Fe/GaN film in oxygen [4,5] or by growing Fe_3O_4 onto a Ga_2O_3 buffer layer [6]. As for the metastable ε-Fe_2O_3—the most intriguing member of the iron oxide family—most works deal with randomly oriented nanoparticles [7–9]. Only few works report epitaxial growth of ε-Fe_2O_3 layers on STO, Al_2O_3, and YSZ [10–13].

Following our earlier papers [14,15], we report here the recent progress in epitaxial stabilization of the four structurally and magnetically different iron oxide phases (Fe_3O_4,

---

[*] Corresponding author: suturin@mail.ioffe.ru

2475-9953/2018/2(7)/073403(11)

α-Fe_2O_3, γ-Fe_2O_3, and the most exotic ε-Fe_2O_3) in the form of nanometer-sized single crystalline films on GaN(0001) surface. After describing the experimental details and growth technology in Sec. II, the layer morphology is discussed in Sec. III. The identification of the iron oxide phases by electron and x-ray diffraction is presented in Secs. IV and V. Section VI is dedicated to x-ray-absorption (XAS) and x-ray magnetic circular dichroism (XMCD) studies aimed at investigation of the oxidation state and coordination of iron atoms in the ferrimagnetically ordered sublattices. Finally the in-plane magnetization reversal in Fe_xO_y/GaN layers is described in Sec. VII. The common building principles of the iron oxide direct and reciprocal lattices are addressed in the Supplemental Material [1].

II. EXPERIMENT

The iron oxide epitaxial layers were grown onto GaN(0001)/Al_2O_3 (0001) surface by pulsed laser deposition from a Fe_2O_3 target ablated by the KrF excimer laser. The growth of the four distinctly different α-Fe_2O_3, γ-Fe_2O_3, ε-Fe_2O_3, and Fe_3O_4 iron oxides on the GaN(0001) surface has been achieved through controlled variation of substrate temperature, background gas composition, and pressure (see Fig. S1 in the Supplemental Material [1]). The iron oxide deposition in oxygen was shown to result in formation of either the α-Fe_2O_3 phase at lower substrate temperature and pressure ($T = 400$–$600\,^{\circ}$C; $p < 0.02$ mbar) or the exotic ε-Fe_2O_3 phase at elevated temperature and pressure ($T = 800\,^{\circ}$C; $p = 0.2$–0.4 mbar). Growth in nitrogen ($T = 600$–$800\,^{\circ}$C at 0.02–0.2 mbar) led to stabilization of the Fe_3O_4 phase. The γ-Fe_2O_3 films were produced by exposing Fe_3O_4 layers to oxygen at 600–800 °C. The real time control over the oxide layer lattice structure and orientation was carried out by the advanced high-energy electron diffraction (RHEED) three-dimensional (3D) reciprocal space mapping [16]. The raw RHEED patterns were collected during sample azimuthal rotation [17] and then used to construct 3D intensity maps. The planar cuts and orthogonal projections of such maps will be presented throughout this paper to describe the reciprocal space structure. The "side views" (cuts performed perpendicular to the sample surface) are improvements over the traditionally published raw patterns; the less conventional "plan views" (projections along the lines parallel to the surface normal that can be visualized solely by 3D mapping) are very informative for understanding the in-plane reciprocal space structure. It is worth noting that the main aim of the applied 3D mapping technique is to measure and model reflection positions and shapes rather than intensities that are known to be subject to dynamical effects. The x-ray-diffraction (XRD) measurements were carried out *ex situ* at the BL3A beamline of the Photon Factory synchrotron (Tsukuba, Japan). The layer morphology was studied using an ambient air NT-MDT atomic force microscope (AFM) and Jeol JEM-2100F transmission electron microscope (TEM) operated in bright-field imaging mode. The magnetic properties were measured at room temperature (RT) using a longitudinal magneto-optical Kerr effect (MOKE) setup described in [17] as well as using the Quantum Design PPMS vibrating-sample magnetometer (VSM) at RT and 100 K. The XAS and XMCD studies have been carried out at RT at the BL 16 beamline of the Photon Factory synchrotron (Tsukuba, Japan).

III. IRON OXIDE LAYER MORPHOLOGY

The plan-view and cross-section morphology of the initial GaN substrate and the iron oxide films was characterized by AFM and TEM. The initial GaN surface is atomically flat with a step-and-terrace surface (Fig. 1). The iron oxides were shown to form uniform layers on the GaN surface. On the nanometer scale the film surface consists of mounds 15–20 nm in width and 1–3 nm in height (Fig. 1). The flattest surface is achieved for the films grown at 600 °C. Even with the film thickness of

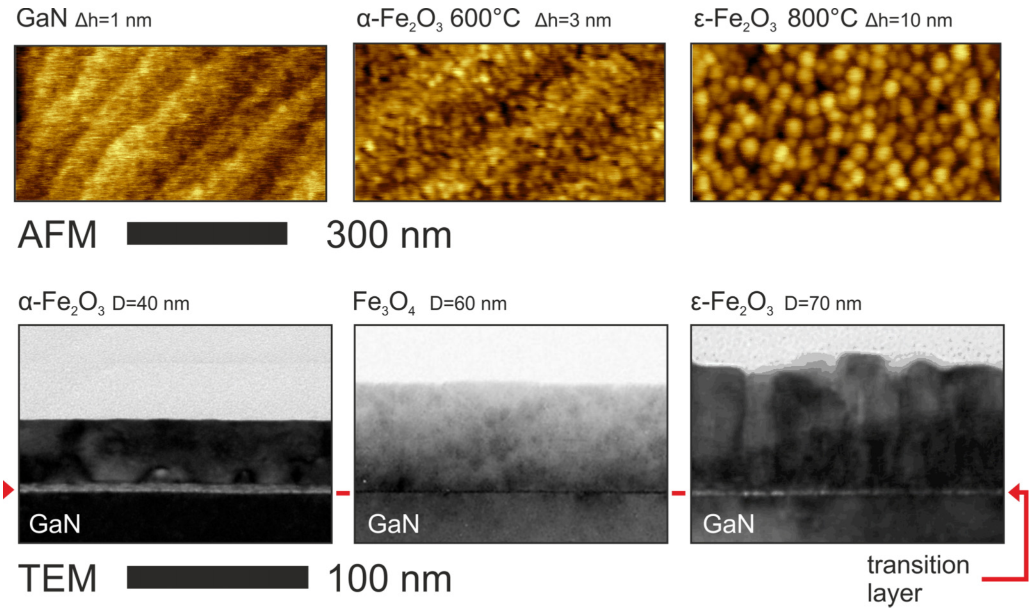

FIG. 1. AFM images (top) show the step-and-terrace GaN surface as well as the typical surface morphology of the iron oxide films grown at 600–800 °C. TEM images (bottom) show cross section of α-Fe_2O_3, ε-Fe_2O_3, and Fe_3O_4 layers. The transition layer at the interface is visible.

40–60 nm, the step-and-terrace pattern of the GaN surface can still be recognized indicating that the surface roughness does not drastically increase. The films grown at 800 °C and high pressure show a more pronounced height variation.

The cross-section TEM images presented in Fig. 1 confirm that the films are continuous. The flattest surface is achieved for the α-Fe_2O_3 layers grown at 600 °C. The highest flatness is likely related to the fact that hematite is the most stable iron oxide phase. The ε-Fe_2O_3 layer grown at 800 °C shows a pronounced columnar structure with column diameter of 30–50 nm. The film surface roughness is a 5–10-nm peak to valley and caused by a slightly different height of the neighboring columns. The film/substrate interface is quite smooth. Interestingly, the TEM images show that a transition layer exists at the iron oxide/GaN interface. When this layer appears lighter in the TEM images it might indicate that it has a lower density or degraded crystalline quality. The thickest transition layer of 5–8 nm is observed for the α-Fe_2O_3 film. In ε-Fe_2O_3 films the transition layer is below 5 nm and the thinnest transition layer is observed in the Fe_3O_4 films. As will be shown in the next section, the existence of an interface layer with a different crystalline structure is well confirmed by diffraction methods. In a separate paper [15] dedicated to the ε-Fe_2O_3/GaN system we have applied polarized neutron reflectometry and secondary ion mass spectroscopy to prove that the transition layer is rich in gallium that might arrive by diffusion from the GaN substrate at elevated growth temperature. The same paper [15] also shows a high-resolution TEM image of the interface region confirming that above the transition layer the crystal structure of the iron oxide film looks as expected. We believe that the temperature driven Ga diffusion from the substrate is somewhat suppressed at lower growth temperatures.

IV. 3D RECIPROCAL SPACE MAPPING BY RHEED

At first glance the trigonal α-Fe_2O_3 ($a = 5.036$ Å, c=13.747 Å), cubic Fe_3O_4/γ-Fe_3O_4/FeO (a=8.399 Å/8.33 Å/4.332 Å), and orthorhombic ε-Fe_2O_3 ($a = 5.089$ Å, $b = 8.780$ Å, $c = 9.471$ Å) have very different symmetries and lattice parameters. However at closer look the building principles of the four lattices are rather similar: in the particular "stacking direction" (which is [111] for Fe_3O_4/γ-Fe_3O_4 and [001] for α-Fe_2O_3/ε-Fe_2O_3) the lattices consist of alternating planes of oxygen and iron (Fig. S2 in Supplemental Material [1]). Noteworthy, the nitrogen planes in GaN are stacked along the [0001] axis similarly to the oxygen planes in the iron oxides. As will be shown below, in the Fe_xO_y/GaN epitaxial system, the iron oxide stacking direction coincides with the GaN [001] surface normal. The oxygen and nitrogen planes get aligned and the O-O/N-N "bonds" within the anion planes become parallel. The four iron oxide phases can be readily identified at the growth stage by carrying out RHEED reciprocal space mapping and analyzing the three orthogonal reciprocal-lattice views as shown in Fig. S3 [1]. Dealing with the four different crystal structures it is convenient to address the reciprocal space cuts as "cut A" parallel and "cut B" perpendicular to the O-O bonds (see Figs. S2 and S3 [1]).

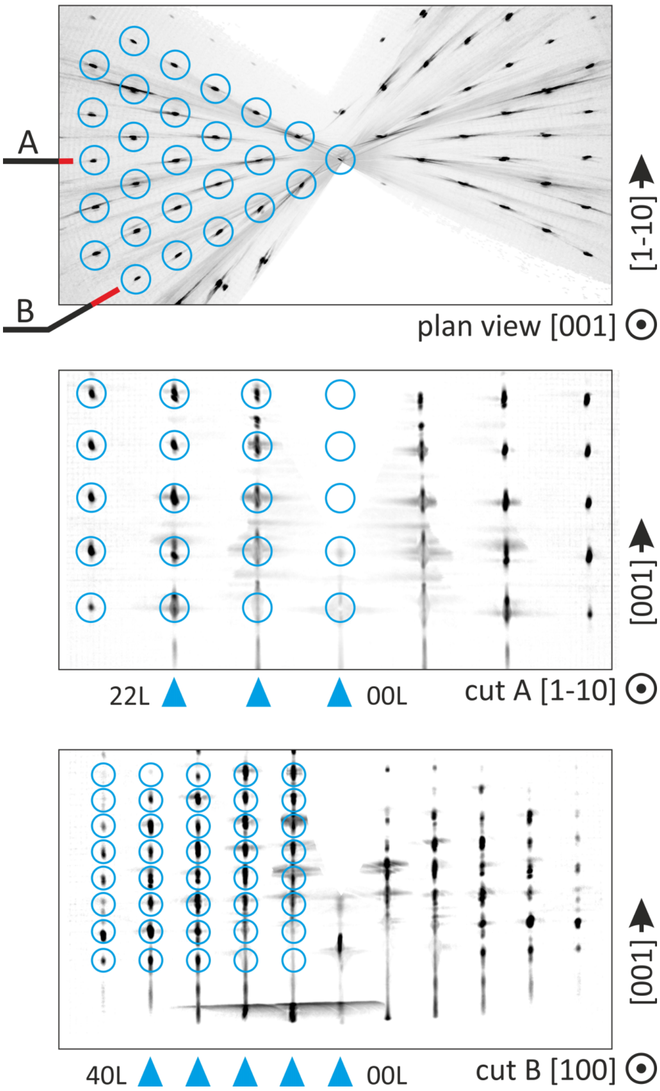

FIG. 2. RHEED reciprocal space map of the clean GaN (0001) substrate prior to the iron oxide deposition. Three orthogonal views including the plan view projection and the two side view reciprocal space cuts A and B are shown in the same scale. The circles represent the modeled GaN reflections. The blue triangles mark lateral positions of the GaN streaks providing a coordinate system convenient for further examination of the iron oxide maps.

A. Iron oxide layer nucleation during initial growth stage

The three orthogonal reciprocal space maps of the initial GaN(0001) surface are shown in Fig. 2 with the modeled reflection positions superimposed. Here and below the modeled reflections are shown only on half of the map to provide a nonobscured view of the experimental data. The GaN reflections close to the shadow edge (low out-of-plane momentum transfer) in cuts A and B are considerably elongated perpendicular to the surface. This is indicative of total external reflection experienced by electrons at a grazing incidence to a flat step-and-terrace substrate surface. The horizontal lines present in cuts A and B are traces of Kikuchi lines that are quite bright for the clean GaN surface. The blue triangles mark lateral positions of the GaN streaks to provide a convenient coordinate system for further iron oxide reciprocal space examination.

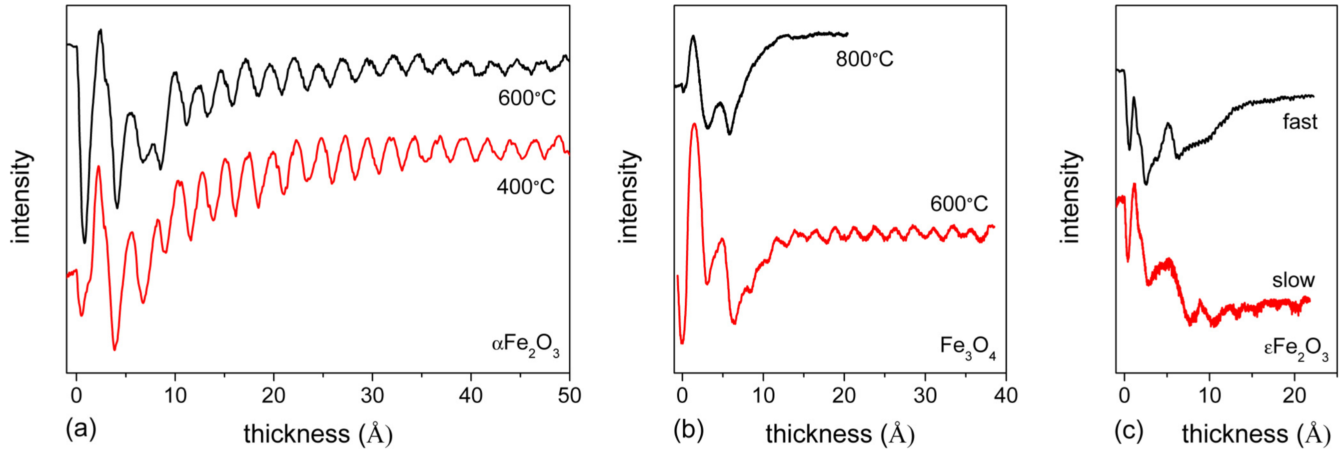

FIG. 3. RHEED specular beam intensity oscillations observed at the beginning of α-Fe_2O_3 (a), Fe_3O_4 (b), and ε-Fe_2O_3 (c) deposition. The most pronounced oscillations corresponding to the layer by layer growth are observed at 600 °C and below. The oscillation period after stabilization is approximately 2.4 Å corresponding to a single O-Fe bilayer.

During deposition of the first few nanometers of the iron oxide, the RHEED streaks become blurry and the distance between them increases, reflecting the decrease of the in-plane periodicity from 3.19 Å in GaN to ~2.9 Å in the iron oxides. At this stage a few-nm-thick transition layer is presumably formed at the interface. The blurry streaks indicate that this layer is disordered likely due to a large number of stacking faults and antiphase boundaries caused by the lattice mismatch.

The iron oxide layer formation is accompanied by RHEED specular beam intensity oscillations (Fig. 3). As it often happens in heteroepitaxy, the first few oscillations show a not easily interpreted wave form. The reason for this is that too many parameters are changed simultaneously during nucleation of the first few monolayers (structure factor of the top layer, refraction potential, surface roughness). Independent on the growth conditions the observed ~2.4-Å oscillation period roughly corresponds to the O-Fe single bilayer (like in α-Fe_2O_3 and FeO) rather than to the O-Fe-O-Fe double bilayer (like in Fe_3O_4 and ε-Fe_2O_3). The most pronounced oscillations are observed during nucleation and growth of α-Fe_2O_3 in 0.02 mbar of oxygen [Fig. 3(a)] at 400 °C (lowest damping) and 600 °C (slightly higher damping). Such behavior corresponds to the layer by layer growth with slow surface roughening. At the growth conditions favorable for nucleation of Fe_3O_4 (0.02–0.2 mbar of nitrogen at 600–800 °C) and ε-Fe_2O_3 (0.2 mbar of oxygen at 800 °C) only few pronounced oscillations are observed at the beginning of the deposition. This corresponds to the Stranski-Krastanov scenario in which the first few monolayers are grown in a layer by layer mode after which the growth switches to the island nucleation regime. A well recognizable diffraction pattern of the particular iron oxide phase appears after deposition of 5–8 nm. The 3D reciprocal space maps of sufficiently thick (20–40 nm) α-Fe_2O_3, Fe_3O_4, γ-Fe_3O_4, and ε-Fe_2O_3 films on GaN are discussed in more detail in the next sections.

B. RHEED 3D mapping of α-Fe_2O_3 layer (hematite)

Upon depositing Fe_2O_3 onto GaN(0001) at 400–600 °C in 0.02 mbar of oxygen the streak arrangement is gradually transformed from the 1 × 1 pattern of the transition layer to the $\sqrt{3} \times \sqrt{3}$ *R*30 pattern of the α-Fe_2O_3 phase (Fig. 4). Depending on the growth rate and temperature, the α-Fe_2O_3 pattern starts to appear after 5–8 nm of deposition.

The observed epitaxial relations are as follows: out-of-plane: GaN[001] ∥ α-Fe_2O_3 [001]; in-plane: GaN[1-10] ∥ α-Fe_2O_3 [110] or [-1-10]. The twofold ambiguity of the in-plane epitaxial relations appears due to the symmetry reasons as the two equally probable orientations may occur when the trigonal α-Fe_2O_3 lattice is placed over the hexagonal GaN lattice. The appearance of the $\sqrt{3} \times \sqrt{3}$ *R*30 set of streaks is readily visible upon comparing the plan view in Fig. 4 to the plan view of the initial GaN surface in Fig. 2. The α-Fe_2O_3 phase can be unmistakably identified by the presence of *N*/3 streaks in the reciprocal space cut A map ([110] zone axis) and no additional features in the reciprocal space cut B map (compare to the sketch in Fig. S3b). Being first weaker than the integer ones, the *N*/3 streaks fully develop after about 10 nm of deposition at which moment they also get modulated in full correspondence with the modeled α-Fe_2O_3 reciprocal-lattice structure. Mind that the reflections of the two 180° domains (shown with different symbols) appear at different coordinates in the cut A map increasing the overall number of spots. The resulting hematite films are insulating, nonmagnetic and have red-orange tint.

C. RHEED 3D mapping of Fe_3O_4 and γ-Fe_3O_4 layers (magnetite and maghemite)

Iron oxide deposition onto GaN at 600–800 °C in 0.02–0.2 mbar of nitrogen leads to stabilization of the Fe_3O_4 phase. Already after 2–3 nm of deposition the 1 × 1 streak pattern of the transition layer starts transforming to the 2 × 2 streak pattern. The latter is characteristic for the spinel cubic lattice of Fe_3O_4 (or γ-Fe_2O_3) with the following epitaxial relations: out-of-plane: GaN[001] ∥ Fe_3O_4 [111]; in-plane: GaN[1-10] ∥ Fe_3O_4 [11-2] or [-1-12]. The twofold ambiguity of the in-plane epitaxial relations is due to the symmetry reasons arising when the cubic iron oxide is placed over hexagonal GaN. The half streaks develop in both cut A and cut B maps (compare

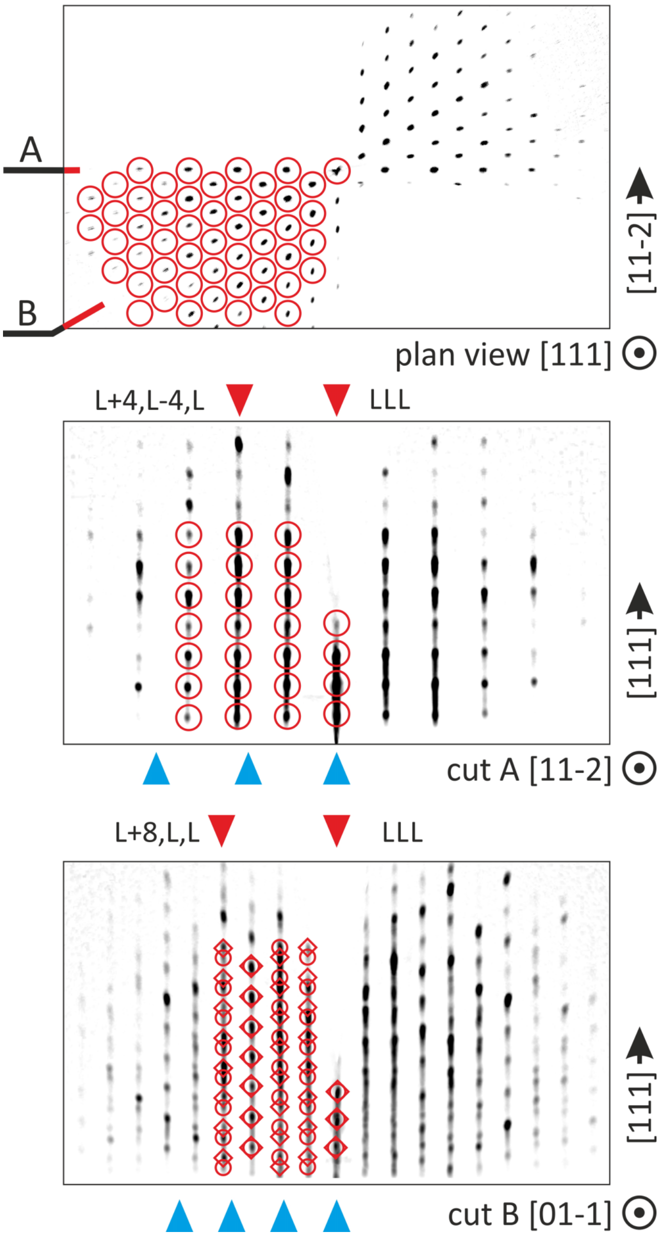

FIG. 4. 3D RHEED reciprocal space maps of 40-nm α-Fe_2O_3 layer. Three orthogonal views including the plan view projection and the two side view reciprocal space cuts A and B are shown in the same scale. The modeled α-Fe_2O_3 reflections are superimposed on the maps. The reflections belonging to the two equivalent domains (shown with different symbols) appear at different coordinates in the "cut A" map. Positions of GaN streaks are shown for scale with blue triangles.

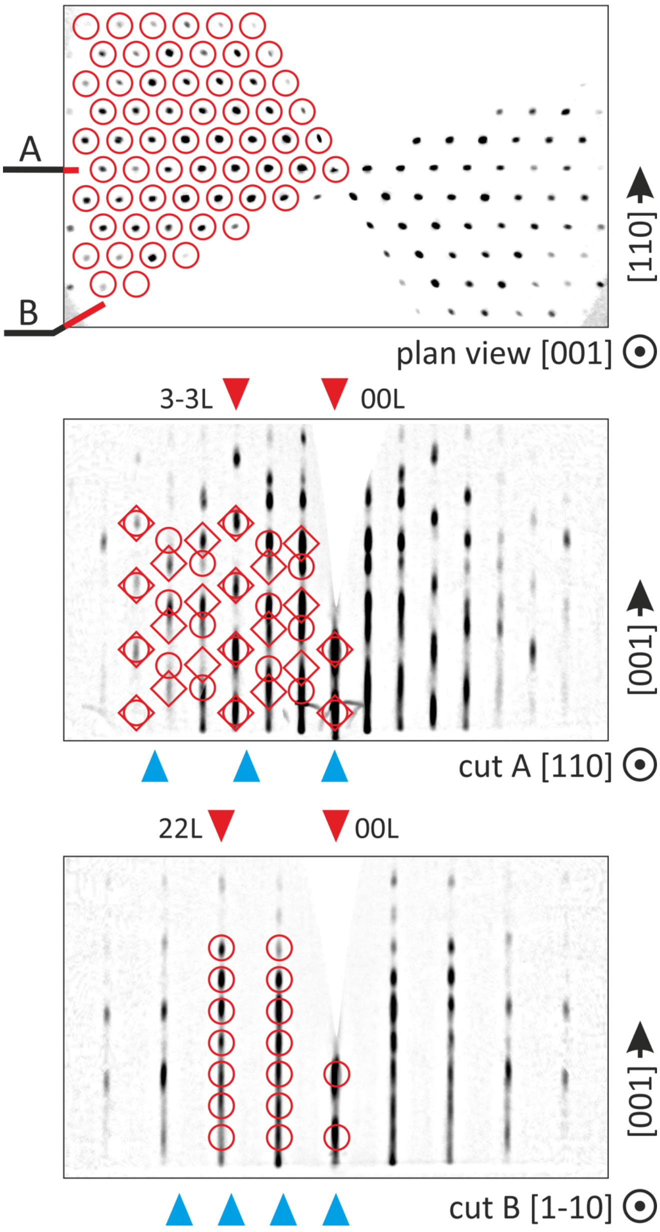

FIG. 5. 3D RHEED reciprocal space maps of 40-nm Fe_3O_4 layer. Three orthogonal views including the plan view projection and the two side view reciprocal space A and B are shown in the same scale. The modeled Fe_3O_4 reflections are superimposed on the maps. The reflections belonging to the two equivalent domains (shown with different symbols) appear at different coordinates in the "cut B" map. Positions of GaN streaks are shown for scale with blue triangles.

to the sketch in Fig. S3b) gradually getting modulated in full resemblance of the expected Bragg reflection positions of Fe_3O_4 or γ-Fe_2O_3 (Fig. 5). The reflections belonging to the two equivalent domains (shown with different symbols) appear at different coordinates in the cut B map. From electron diffraction maps it is almost impossible to distinguish Fe_3O_4 from γ-Fe_2O_3 as both oxides obtain the same lattice structure and almost the same lattice constant. The films grown in nitrogen are identified as magnetite (or at least as magnetite-rich) because they have a distinct gray metallic tint and are electrically conducting at room temperature. The substitution of Fe^{III} ions with Fe^{II} is the direct consequence of the reduced amount of oxygen in the plume.

Interestingly growing in oxygen deficient (reducing) UHV conditions does not lead to Fe_3O_4 stabilization. A nitrogen background atmosphere at a pressure no less than 0.02 mbar is needed to stabilize magnetite, otherwise α-Fe_2O_3 would eventually grow. Increasing nitrogen pressure to 0.2 mbar leads to faster magnetite nucleation and subsequently brighter diffraction patterns. The probable explanation could be that nitrogen acts as a sort of oxygen absorber forming NOx compounds. The same approach of using nitrogen background atmosphere [18] has proved efficient to grow Fe_3O_4 on MgO(001) whereas growing in oxygen results in the γ-Fe_2O_3 phase.

The observed Fe_3O_4/GaN epitaxial relations are in agreement with those discussed in Ref. [4] where Fe_3O_4 films on GaN were obtained by oxidation of Fe/GaN layers. Apparently iron oxidation technology leads to formation of a partially disordered magnetite film as in the diffraction patterns presented in Ref. [4] the half order streaks are considerably weaker than the integer ones. In contrast to this, our magnetite films are fully ordered as confirmed by uniform streak brightness. Upon exposing the Fe_3O_4/GaN films to oxygen at 600–800 °C we have observed an immediate transformation of Fe_3O_4 to γ-Fe_2O_3 accompanied by a change of color from dark gray to light ochre and the drop of conductivity to infinity. The Fe_3O_4-γ-Fe_2O_3 transformation produced no drastic changes in the diffraction pattern and was shown to affect the top 20 nm of the film. To grow thicker maghemite layers, the growth/oxidation procedure had to be repeated multiple times. It is noteworthy that the magnetite-maghemite transformation is expected to proceed through creation of iron octahedral vacancies, that is, iron must travel out of the film volume to meet oxygen at the surface. This process would involve not only volume transformation but also crystallization of extra material at the surface. Though the lattice structure and epitaxial relations do not change upon oxidation, a certain amount of surface roughening upon Fe_3O_4 oxidation is observed by AFM.

D. RHEED 3D mapping of ε-Fe_2O_3 layers

The most unusual result of the present investigation is epitaxial stabilization of the metastable ε-Fe_2O_3 phase on GaN surface. The ε-Fe_2O_3 polymorph was shown to grow on GaN in 0.2 mbar of oxygen at 800 °C. The diffraction pattern characteristic for ε-Fe_2O_3 appears after about 4–5 nm of deposition and stays stable up to the maximum tested thickness of 40 nm. The unmistakable characteristic of the ε-Fe_2O_3 phase is the appearance of reflections on the $N/6$ streaks in the cut-A reciprocal space maps ([100] zone axis) (Fig. 6).

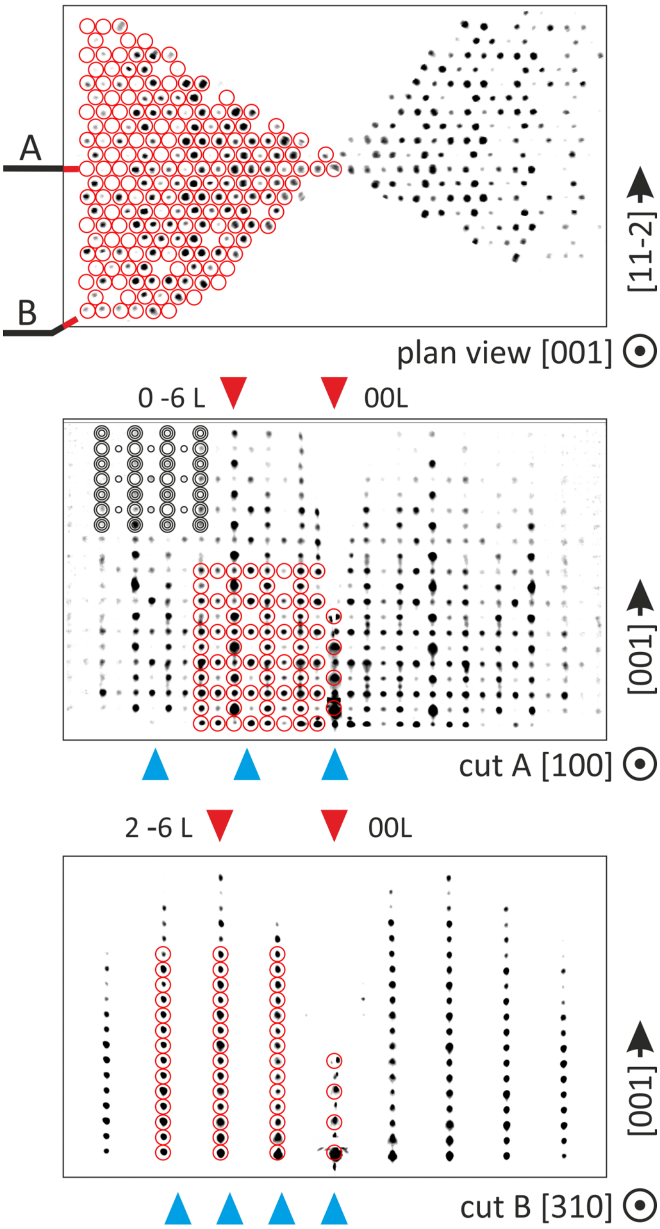

FIG. 6. 3D RHEED reciprocal space map measured for ε-Fe_2O_3 layer. Three orthogonal views including the plan view projection and the two side view reciprocal space cuts A and B are shown in the same scale. The modeled ε-Fe_2O_3 reflections are superimposed on the maps. The reflections belonging to the three equivalent domains (shown with circles of different radius) appear at different coordinates in the "cut A" map. Positions of GaN streaks are shown for scale with blue triangles.

The following epitaxial relations are observed. Out-of-plane: GaN[001] ∥ ε-Fe_2O_3 [001]; in-plane: GaN[1-10] ∥ ε-Fe_2O_3 [100] or [-1-10] or [-110]. The threefold ambiguity of the in-plane epitaxial relations appears due to symmetry reasons when placing orthorhombic ε-Fe_2O_3 lattice over hexagonal GaN lattice. Noteworthy, the "b" lattice parameter of ε-Fe_2O_3 is $\sqrt{3}$ times larger than the "a" lattice parameter. This accounts for the coincidence of a great deal of reflections upon 120° rotation around the surface normal. In some ε-Fe_2O_3 films a faint trace of α-Fe_2O_3 is observed. The ε-Fe_2O_3 films have an ochre tint and are insulating.

V. X-RAY-DIFFRACTION STUDIES

X-ray-diffraction was used in this study as a tool complementary to RHEED as the latter technique probes only a thin near-surface region, has a limited out-of-plane resolution, and cannot rule out recrystallization effects possibly occurring deep inside the film during or after growth. Figure 7 shows intensity distribution along the specular crystal truncation rods measured in 40-nm iron oxide films. The observed Bragg peaks are in good agreement with the epitaxial relations observed by RHEED. An accurate evaluation of the out-of-plane lattice periodicity has been done. As discussed in the Supplemental Material [1], this periodicity is linked to the distance between the oxygen planes and varies from phase to phase due to

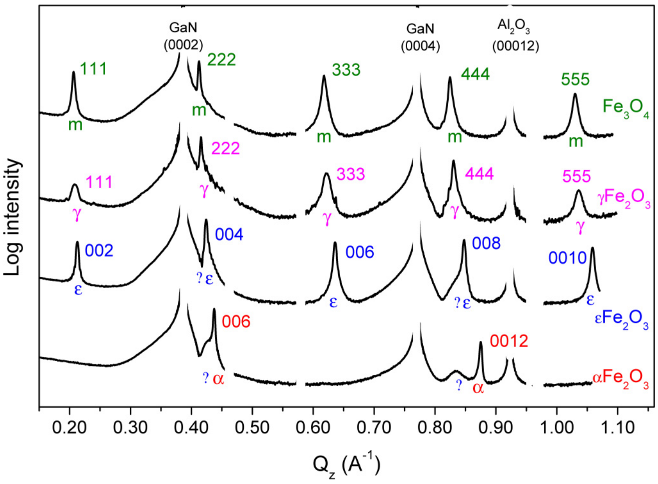

FIG. 7. XRD specular intensity profiles measured in 40-nm thick Fe_3O_4, γ-Fe_2O_3, ε-Fe_2O_3, and α-Fe_2O_3 epitaxial layers on GaN(0001). Apart from the brightest peaks belonging to GaN and Al_2O_3 distinct Bragg reflections of the corresponding iron oxide phases are present. In ε-Fe_2O_3 and α-Fe_2O_3 samples, additional two peaks corresponding to the transition layer are clearly visible (labeled with question mark).

different stacking order and different arrangement of the O_h and T_d iron sites. Moreover in γ-Fe_2O_3, Fe_3O_4 and ε-Fe_2O_3 the monolayer contains two oxygen planes leading to a twice denser sequence of reflections than in α-Fe_2O_3 in which the monolayer contains only one oxygen plane. It follows from the shown profiles that the Fe_3O_4 and γ-Fe_2O_3 (111) layers are slightly expanded perpendicular to the surface while the α-Fe_2O_3 (0001) and ε-Fe_2O_3 (001) layers are slightly compressed. The measured distances between the oxygen planes (d) and the corresponding lattice parameters (a, c) are listed in Table I. The lattice parameters for Fe_3O_4 and γ-Fe_2O_3 are calculated assuming that the lattice remains cubic. Interestingly, the two nonhematite peaks (labeled with question marks in Fig. 7) are present in the α-Fe_2O_3 specular profile. These peaks are much wider and weaker than the main α-Fe_2O_3 reflections. Their contribution was shown to decrease with film thickness indicating that they originate from a thin layer located at the GaN interface.

Most likely the extra peaks are the fingerprint of the transition layer observed earlier by TEM and RHEED. The transition layer peaks are very well distinguished in the α-Fe_2O_3 layer. The peak width corresponds to a 5-nm film in good agreement with RHEED and TEM. In the ε-Fe_2O_3 layers a small hump on the low-q side of the 008 reflection is approximately at the same place and of the same width as the transition layer reflection in α-Fe_2O_3. In Fe_3O_4 and γ-Fe_2O_3 the transition layer peak cannot be distinguished likely because this layer is few times thinner than in α-Fe_2O_3. In agreement with RHEED oscillations the out-of-plane interlayer spacing in the transition layer is 2.395 Å (close to the undistorted γ-Fe_2O_3) corresponding to a single rather than double O-O monolayer spacing. Interestingly, the Bragg peaks of the transition layer show interference with the high-Q_z slopes of the GaN 0002 and GaN 0004 reflections being an indication of a sharp interface. It becomes clear from the XRD studies that the iron oxide films are single phase with the out-of-plane interlayer spacing slightly modified with respect to the corresponding bulk values. No postgrowth phase conversion has been observed so far.

VI. X-RAY ABSORPTION SPECTROSCOPY AND MAGNETIC CIRCULAR DICHROISM

X-ray absorption and x-ray magnetic circular dichroism have been applied in this work to probe oxidation states and coordination of the Fe atoms in ferrimagnetically ordered sublattices of the studied iron oxides. While the diffraction techniques are sensitive to the crystal structure, the soft x-ray spectroscopy is able to prove that the iron atoms are in the expected chemical environment. Most important is that the method is sensible to the noncrystalline fractions (e.g., segregated metallic iron) that cannot be observed with diffraction techniques. The L_{23} spectra of the transition metals originate from the dipole-allowed $2p$-$3d$ transitions and consist of L_3 and L_2 main peaks resulting from the spin-orbit coupling. In the iron oxides the ligand field of the oxygen atoms splits the Fe $3d$ into e_g and t_{2g} orbitals providing a highly sensitive probe of coordination environment and magnetization of individual sublattices. The Fe L_{23} XAS spectra measured in the iron oxide films grown on GaN are shown in Fig. 8 together with the reference spectra adopted from [19–21]. In all the studied samples the L_3 peak exhibits two major components: a main peak at 709.5 eV and a satellite at 708 eV. This spectral shape is characteristic of the oxidized iron as opposed to the metallic one [22]. In 40 nm α-Fe_2O_3 film the splitting is the most pronounced originating from the pure octahedral coordination of Fe^{III} ions in hematite [19,22,23]. In 40-nm γ-Fe_2O_3 and ε-Fe_2O_3 films the L_3 splitting is less pronounced in agreement with other works dedicated to γ-Fe_2O_3 [19,23,24] and ε-Fe_2O_3 [20]. While the separation

TABLE I. Lattice parameters of the iron oxide films evaluated from the specular XRD profiles. To stress similarities in oxygen sublattice structure, the spacing between O planes is given in comparison to the bulk values.

Material	O planes in one monolayer	O-O layer spacing d (Å)		Out-of-plane lattice expansion (%)	Lattice constant (Å)	
		Measured	Bulk		Calculated	Bulk
Fe_3O_4	2	2.428	2.424	+ 0.1	$a = 2\sqrt{3}d = 8.41$	8.398
γ-Fe_2O_3	2	2.411	2.405	+ 0.3	$a = 2\sqrt{3}d = 8.354$	8.33
ε-Fe_2O_3	2	2.360	2.368	−0.3	$c = 4d = 9.438$	9.471
α-Fe_2O_3	1	2.285	2.291	−0.3	$c = 6d = 13.708$	13.747
tr. layer	1	2.395				

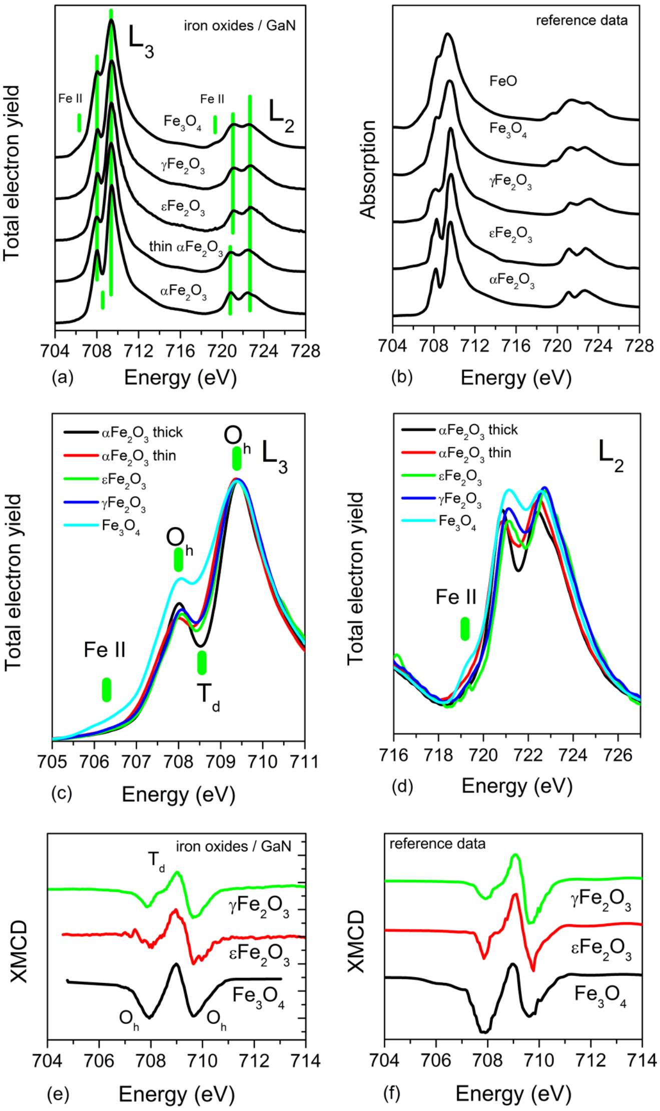

FIG. 8. X-ray-absorption spectra obtained from 40-nm-thick iron oxide epitaxial films on GaN showing the full L_{23} spectral range (a) and the detailed L_3 and L_2 spectra (c),(d). Reference data adopted from [19–21] are shown for comparison (b). The features in the spectra belonging to Fe II and Fe III as well as to the octahedral (O_h) and tetrahedral (T_d) iron sites are marked. XMCD spectra obtained from the iron oxide epitaxial films on GaN (e). Reference data adopted from [19–21] are shown for comparison (f).

between the 708- and 709.5-eV components is the same as in α-Fe_2O_3, the intensity drop between the peaks becomes less pronounced due to the presence of a Fe^{III} T_d peak right in the middle between the two O_h peaks.

Interestingly the same shape of L_3 edge as in γ-Fe_2O_3 and ε-Fe_2O_3 is observed in the 5-nm transition layer (preceding α-Fe_2O_3 formation) indicating the presence of T_d sites near the interface. The nonhematite nature of the transition layer is in agreement with the diffraction data. It is noteworthy that the only existing work describing the x-ray-absorption in ε-Fe_2O_3 [20], shows a spectrum that resembles more α-Fe_2O_3 with high contrast L_3 splitting [Fig. 8(b)]. Our data show more resemblance to γ-Fe_2O_3 which seems more natural as in ε-Fe_2O_3 (as opposed to α-Fe_2O_3) a T_d iron sublattice exists in addition to the three distorted O_h sublattices. In contrast to the pure trivalent oxides, our Fe_3O_4 films exhibit an extra shoulder at 706.5 eV and a considerably higher satellite at 709.5 eV. These features are known to be characteristic of O_h Fe^{II} sites in magnetite [22–27]. The shape of the L_2 peaks in the studied iron oxide films bears some similarity to that of the L_3 peaks, exhibiting the Fe^{II} low-energy shoulder in Fe_3O_4 and a better resolved satellite in α-Fe_2O_3.

The XMCD measurements at Fe L_{23} edge have been carried out to investigate magnetic nature of Fe sublattices in comparison to the corresponding bulk iron oxides. Within the experiment accuracy no dichroic signal has been detected in the expected to be weak ferrimagnetic α-Fe_2O_3 films. The XMCD spectra of the other three iron oxides compared to the reference spectra are shown in Figs. 8(e) and 8(f). The general trend is that the L_3 XMCD spectra are dominated by the two negative peaks and a positive peak in between. The negative peaks correspond to the Fe magnetic moments in O_h sites aligned parallel to the field. The positive peak corresponds to the Fe magnetic moments in T_d site aligned antiparallel to the field. In the pure Fe^{III} oxides (γ-Fe_2O_3, ε-Fe_2O_3) the higher energy O_h peak is dominant [compare to the reference spectra in Fig. 8(f) adopted from [19,20]]. In the mixed II/III Fe_3O_4 the low-energy peak is higher and wider due to the presence of the O_h Fe^{II} ions [4,28]. The net magnetization in ferrimagnetic iron oxides results from the antiparallel alignment of magnetic moments at the octahedral and tetrahedral Fe sites. In contrast to the XMCD spectra of metallic iron for which the L_3 peaks measured at opposite helicities show different heights, in iron oxides these peaks are shifted in energy. To summarize, the soft x-ray-absorption spectroscopy has confirmed that the iron atoms reside in the expected crystallographic environment and have the expected oxidation state; moreover the films may be considered chemically pure. For all the studied cases the distinction can be made between the tetrahedrally and octahedrally coordinated iron atoms both in XAS and XMCD spectra. Interestingly the transition layer was found to contain tetrahedrally coordinated iron.

VII. IN-PLANE MAGNETIZATION REVERSAL IN THE IRON OXIDE LAYERS

In-plane magnetization reversal curves of the iron oxide layers have been investigated by MOKE and VSM to compare the magnetic properties of the grown films to those of the same materials in bulk or nanoparticle form. Figure 9(a) emphasizes the big difference of the typical $M(H)$ curves measured in Fe_3O_4, α-Fe_2O_3, γ-Fe_2O_3, and ε-Fe_2O_3 layers.

A. Epsilon ferrite

In ε-Fe_2O_3 (001) layers the easy magnetization [100] axis lies in the film plane accounting for the hard magnetic nature of the in-plane magnetization curves. Such curves have been measured by VSM showing saturation of 110 emu/cc, coercivity of 8 kOe, and saturation field of 20 kOe [Fig. 9(c)]. These values are typical for ε-Fe_2O_3 nanoparticles and films reported by different authors [7–13]. Similar to the other reports we observe loops of wasp-waist shape exhibiting abrupt magnetization jumps at zero magnetic field. The wasp-waist loop is explained by the coexistence of magnetically hard and soft components in ε-Fe_2O_3 film. An example of loop decomposition is shown in Fig. 9(c). The hard magnetic component loop shape is in agreement with the idea of ε-Fe_2O_3 film consisting of domains with three possible orientations of the easy magnetization [100] axis at 120° to each other. In this configuration the magnetic field is always at an angle with the easy axis of at least two domains which makes the magnetization loops nonrectangular.

The origin of the soft component loop is arguable—different works relate it to the presence of magnetite or maghemite impurities, to the antiphase boundaries, or to the magnetically soft behavior of the undistorted O_h sublattices. According to our diffraction measurements, hematite is the only parasitic phase that can be present to some extent at the near surface region of the nonoptimally grown ε-Fe_2O_3 films. However due to the negligibly small magnetic moment, hematite cannot account for the zero-field magnetization jumps of up to 40 emu/cc. Our polarized neutron reflectometry study [15] has shown that the soft loop is likely related to the Ga-rich transition layer.

B. Hematite

We have also looked for the presence of weak ferromagnetism in α-Fe_2O_3 films grown on GaN. At above the Morin transition temperature of 250 K the canted antiferromagnetically coupled magnetic moments in α-Fe_2O_3 are known to result in spontaneous magnetization lying in the (0001) basal plane [29,30]. As the canting angle is just a fraction of a degree, the resulting magnetic moment is very small—of the order of few emu/cc. Such small magnetization could not be detected in our XMCD experiments. Neither was VSM capable to accurately measure a magnetization loop in a 40-nm α-Fe_2O_3 film. A very noisy VSM loop in Fig. 9(a) is shown to emphasize the tiny <5 emu/cc saturation magnetization in α-Fe_2O_3 compared to the much larger 110 emu/cc value measured for ε-Fe_2O_3. Interestingly, despite the small magnetic moment, a very pronounced Kerr polarization rotation was observed in the studied α-Fe_2O_3 films [Fig. 9(a)]. The anomalously strong magneto-optical effects in weak ferromagnets are known to occur due to dependence on the antiferromagnetic vector rather than just on the total magnetization [31]. In the very early works linear magnetic birefringence [32] and Kerr effect [33] in hematite have been reported. The Kerr rotation in hematite is claimed to be as strong as in the rare-earth iron garnets [34] and can be used to visualize magnetic domains with polarization microscopy [35]. The observed MOKE loop shape in our α-Fe_2O_3/GaN films is in general agreement with the VSM magnetization curves reported by other authors. Bulk samples which contain hematite single domain nanoparticles usually exhibit coercivity of a few kOe and saturation field above 20 kOe [36–38]. Such magnetization behavior is in contrast with the properties of the large natural hematite crystals that have much lower coercive field of 3–30 Oe [39]. The main source of the high coercivity in nanoparticles is believed to be the magnetoelastic anisotropy that can be associated with subparticle structure, strain, or twinning [40,41].

C. Magnetite and maghemite

The MOKE magnetization loops of 20-nm Fe_3O_4 layers grown in a range of growth conditions (600–800 °C in 0.02–0.5 mbar of nitrogen) exhibit coercivity of 300–400 Oe and remanence of about 70% of the saturation value [Fig. 9(b)]. Very similar magnetization loops have been observed in Fe_3O_4 films grown by PLD on Si(001) [42]. A similar loop shape with somewhat lower coercivity of 120–150 Oe was observed in Fe_3O_4/GaN(0001) films grown by oxidizing a few-nm-thick iron layer [4]. In our samples the Kerr rotation of the γ-Fe_2O_3 layers is typically 1.5 times weaker compared to that of Fe_3O_4. As the magnetite layer thickness is decreased from 20 to 6 nm and further to 2 nm the saturation field gets lower while the remanent magnetization disappears resembling approach to the superparamagnetic behavior.

The aforementioned thickness dependence for the magnetite films indicates that at the nucleation stage the film consists of magnetically noninteracting small grains. The high coercive field observed in α-Fe_2O_3 and ε-Fe_2O_3 films is also indicative of the single domain particles rather than a multiple domain film. It is well known that the maximum coercivity for a given material occurs within its single domain range

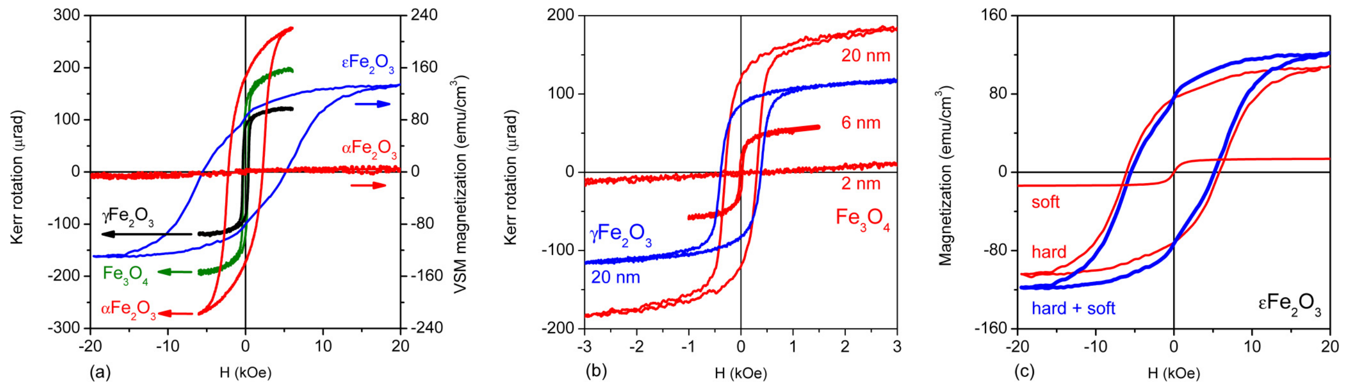

FIG. 9. (a) A comparison chart of in-plane magnetization reversal curves measured by longitudinal Kerr effect at $\lambda = 405$ nm and VSM for 40-nm-thick α-Fe_2O_3, Fe_3O_4, γ-Fe_2O_3, and ε-Fe_2O_3 films on GaN. The drastic variation of iron oxide magnetic properties is present. (b) In-plane MOKE magnetization curves in Fe_3O_4 and γ-Fe_2O_3 films of different thickness showing gradual transition from small superparamagnetic to large ferromagnetic grains. (c) In-plane VSM magnetization curve in 40-nm ε-Fe_2O_3 film decomposed into magnetically hard and magnetically soft components.

where the magnetization reverses via synchronous magnetic moment rotation of the whole grain. The critical size for the single domain behavior is estimated to be about 80 nm for magnetite [43] and 20–100 micrometers for hematite (20-100 micrometers) [44]. The mounds observed by AFM in our films are within the single domain region.

VIII. SUMMARY

In the present work we have investigated the tunable polymorphism of epitaxial iron oxides on GaN(0001) surface. Four crystallographically and magnetically different iron oxide phases—Fe_3O_4, γ-Fe_2O_3, ε-Fe_2O_3 and α-Fe_2O_3—have been stabilized by means of the single target laser molecular beam epitaxy (MBE) technology by controllable variation of substrate temperature, buffer gas composition, and pressure. The epitaxial control over the iron oxide polymorphism on GaN has been explained by the common building principles of the iron oxide lattices. Our RHEED and XRD studies have shown that the iron oxides crystallize with the oxygen planes parallel to the GaN (0001) surface and the in-plane epitaxial relations defined by the coincidence of the in-plane O-O and N-N vectors. With these epitaxial relations, the iron oxide phases may be easily switched during the growth in a way similar to the ABC-ABC/AB-AB-AB stacking switching observed in fcc/hcp lattices [45]. The lower symmetry of the iron oxide planes compared to GaN accounts for multiple possible in-plane orientations—two for Fe_3O_4, γ-Fe_2O_3, α-Fe_2O_3 and three for ε-Fe_2O_3. This ambiguity together with the few times larger in-plane lattice periodicity of the iron oxide is supposed to be responsible for the appearance of phase shifted regions during the film nucleation stage. The thick films are shown to be uniform with low surface roughness and are supposed to consist of single crystalline columns separated by antiphase boundaries.

An important component of the Fe_xO_y/GaN technology is the transition layer that forms at the initial growth stage on GaN. This layer has the out-of-plane periodicity coincident with the single O-O interplane distance and the in-plane periodicity of the single hexagonal oxygen plane. The longer in-plane periodicities characteristic of the bulk iron oxides are not present at this stage as shown by diffraction. The transition layer consists of small regions in phase with GaN but out of phase with each other. As confirmed by TEM and RHEED, the defect rich transition layer is the thickest in α-Fe_2O_3 and ε-Fe_2O_3 films and much thinner in Fe_3O_4 layers. Interestingly the transition layer was shown to contain tetrahedrally coordinated iron.

The observed surface morphology might be the result of the island nucleation and coalescence mechanism. This kind of growth was reported earlier for ε-Fe_2O_3 layers on STO and YSZ [11–13]. The columnar structure explains well the magnetic behavior of the iron oxide films on GaN suggesting that columns are single magnetic domains. Hard magnetic behavior of ε-Fe_2O_3 films and much softer behavior of Fe_3O_4 and γ-Fe_2O_3 films are in agreement with the other works. Decreasing film thickness was shown to result in appearance of superparamagnetic loop shape due to the small size of the single domain particles present at the nucleation stage. Interestingly the rather hard magnetic behavior was also observed in weak ferrimagnetic α-Fe_2O_3 films in agreement with various studies of hematite nanoparticles. The very low total magnetization in thin α-Fe_2O_3 films makes it difficult to apply VSM. However the rather high magneto-optical effects made it possible to monitor magnetization reversal in α-Fe_2O_3 films by means of MOKE. The x-ray-absorption spectra measured at the *L* edge of iron were shown to be in good agreement with the reference spectra obtained in a number of works describing different iron oxides in bulk and nanocrystalline forms. This is an important proof of the chemical pureness of the grown films. Distinguishing iron coordination and oxidation state for different oxides makes possible further studies of the individual magnetic sublattices in the ferromagnetic iron oxides by means of XMCD. This is especially challenging to be carried out for the scarcely studied epsilon ferrite obtaining four different iron sublattices.

In general the obtained results are believed to be helpful in clarifying the influence of technological parameters on the laser MBE process and in getting hold of the mechanisms guiding the particular phase choice during film nucleation and growth. The demonstrated flexibility in iron oxide phase stabilization by laser MBE makes it possible to predict that a similar approach may be applied to the growth on the AlGaN (0001) surface. More complex compounds like $Fe_xGa_yAl_{1-x-y}O_3$ can be also tried for the role of the ferromagnetic layer. Combining epitaxial layers of magnetically ordered materials with GaN is supposed to present potential interest for designing different (opto-) electronic and spintronic devices for room-temperature operation.

ACKNOWLEDGMENTS

The authors wish to acknowledge W. V. Lundin for providing GaN/Al_2O_3 wafers, and the beamline staff at PF for kind assistance in conducting experiments. Beam time at PF was granted for Projects No. 2014G726, No. 2014G725, and No. 2016G684. TEM studies have been performed on the equipment of “Material science and characterization in advanced technology” Federal Joint Research Center supported by the Ministry of Education and Science of the Russian Federation (id RFMEFI62117X0018). Support for conducting synchrotron measurements has been received from Nagoya University. This work has been supported by Russian Science Foundation (Project No. 17-12-01508) in part related to development of the growth technology and by Russian Foundation for Basic Research Grant No. 18-02-00789 in part related to the studies of epsilon ferrite growth and magnetic properties.

---

[1] See Supplemental Material at http://link.aps.org/supplemental/10.1103/PhysRevMaterials.2.073403 for the comprehensive description of the bulk lattice structures and magnetic characteristics of α-Fe_2O_3, Fe_3O_4, γ-Fe_2O_3, and ε-Fe_2O_3.

[2] E. Parsianpour, M. Gholami, N. Shahbazi, and F. Samavat, Surf. Interface Anal. **47**, 612 (2015).

[3] P. Li, C. Xia, Z. Zhu, Y. Wen, Q. Zhang, H. N. Alshareef, and X.-X. Zhang, Adv. Funct. Mater. **26**, 5679 (2016).

[4] P. K. J. Wong, W. Zhang, X. G. Cui, Y. B. Xu, J. Wu, Z. K. Tao, X. Li, Z. L. Xie, R. Zhang, and G. van der Laan, Phys. Rev. B **81**, 035419 (2010).
[5] X. Zou, J. Wu, P. K. J. Wong, Y. B. Xu, R. Zhang, Y. Zhai, C. Bunce, and R. W. Chantrell, J. Appl. Phys. **109**, 07D341 (2011).
[6] Z. Xu, S. Huang, K. Tang, S. Gu, S. Zhu, J. Ye, M. Xu, W. Wang, and Y. Zheng, Appl. Surf. Sci. **388**, 141 (2016).
[7] J. López-Sánchez, A. Serrano, A. Del Campo, M. Abuín, O. Rodríguez de la Fuente, and N. Carmona, Chem. Mater. **28**, 511 (2016).
[8] S.-I. Ohkoshi, A. Namai, K. Imoto, M. Yoshikiyo, W. Tarora, K. Nakagawa, M. Komine, Y. Miyamoto, T. Nasu, S. Oka, and H. Tokoro, Sci. Rep. **5**, 14414 (2015).
[9] A. Namai, M. Yoshikiyo, K. Yamada, S. Sakurai, T. Goto, T. Yoshida, T. Miyazaki, M. Nakajima, T. Suemoto, H. Tokoro, and S. Ohkoshi, Nat. Commun. **3**, 1035 (2012).
[10] M. Gich, J. Gazquez, A. Roig, A. Crespi, J. Fontcuberta, J. C. Idrobo, S. J. Pennycook, M. Varela, V. Skumryev, and M. Varela, Appl. Phys. Lett. **96**, 112508 (2010).
[11] M. Gich, I. Fina, A. Morelli, F. Sánchez, M. Alexe, J. Gàzquez, J. Fontcuberta, and A. Roig, Adv. Mater. **26**, 4645 (2014).
[12] T. M. N. Thai, D. T. Nguyen, N.-S. Lee, J.-S. Rhyee, J. Song, and H.-J. Kim, J. Appl. Phys. **120**, 185304 (2016).
[13] L. Corbellini, C. Lacroix, C. Harnagea, A. Korinek, G. A. Botton, D. Ménard, and A. Pignolet, Sci. Rep. **7**, 3712 (2017).
[14] S. M. Suturin, A. M. Korovin, V. V Fedorov, S. V Gastev, V. P. Volkov, Y. Y. Petrova, M. Tabuchi, and N. S. Sokolov, in *24th International Symposium "Nanostructures: Physics and Technology"* (Academic University Publishing, St. Petersburg, 2016), pp. 37–38.
[15] V. Ukleev, S. Suturin, T. Nakajima, T. Arima, T. Saerbeck, T. Hanashima, A. Sitnikova, D. Kirilenko, N. Yakovlev, and N. Sokolov, Sci. Rep. **8**, 8741 (2018).
[16] S. M. Suturin, A. M. Korovin, V. V. Fedorov, G. A. Valkovsky, M. Tabuchi, and N. S. Sokolov, J. Appl. Crystallogr. **49**, 1532 (2016).
[17] B. B. Krichevtsov, S. V Gastev, S. M. Suturin, V. V Fedorov, A. M. Korovin, V. E. Bursian, A. G. Banshchikov, M. P. Volkov, M. Tabuchi, and N. S. Sokolov, Sci. Technol. Adv. Mater. **18**, 351 (2017).
[18] S. Suturin, A. Kaveev, A. Korovin, V. Fedorov, M. Sawada, and N. Sokolov, J. Appl. Crystallogr. (2018), doi:10.1107/S1600576718007823.
[19] D. H. Kim, H. J. Lee, G. Kim, Y. S. Koo, J. H. Jung, H. J. Shin, J.-Y. Kim, and J.-S. Kang, Phys. Rev. B **79**, 033402 (2009).
[20] Y.-C. Tseng, N. M. Souza-Neto, D. Haskel, M. Gich, C. Frontera, A. Roig, M. van Veenendaal, and J. Nogués, Phys. Rev. B **79**, 094404 (2009).
[21] K. Kuepper, I. Balasz, H. Hesse, A. Winiarski, K. C. Prince, M. Matteucci, D. Wett, R. Szargan, E. Burzo, and M. Neumann, Phys. Status Solidi **201**, 3252 (2004).
[22] T. J. Regan, H. Ohldag, C. Stamm, F. Nolting, J. Lüning, J. Stöhr, and R. L. White, Phys. Rev. B **64**, 214422 (2001).
[23] D. Peak and T. Regier, Environ. Sci. Technol. **46**, 3163 (2012).
[24] L. Signorini, L. Pasquini, F. Boscherini, E. Bonetti, I. Letard, S. Brice-Profeta, and P. Sainctavit, Phys. Rev. B **74**, 014426 (2006).
[25] J. Chen, D. J. Huang, A. Tanaka, C. F. Chang, S. C. Chung, W. B. Wu, and C. T. Chen, Phys. Rev. B **69**, 085107 (2004).
[26] W. Q. Liu, Y. B. Xu, P. K. J. Wong, N. J. Maltby, S. P. Li, X. F. Wang, J. Du, B. You, J. Wu, P. Bencok, and R. Zhang, Appl. Phys. Lett. **104**, 142407 (2014).
[27] D. J. Huang, C. F. Chang, H.-T. Jeng, G. Y. Guo, H.-J. Lin, W. B. Wu, H. C. Ku, A. Fujimori, Y. Takahashi, and C. T. Chen, Phys. Rev. Lett. **93**, 077204 (2004).
[28] W. Q. Liu, M. Y. Song, N. J. Maltby, S. P. Li, J. G. Lin, M. G. Samant, S. S. P. Parkin, P. Bencok, P. Steadman, A. Dobrynin, Y. B. Xu, and R. Zhang, J. Appl. Phys. **117**, 17E121 (2015).
[29] I. Dzyaloshinsky, J. Phys. Chem. Solids **4**, 241 (1958).
[30] T. Moriya, Phys. Rev. **117**, 635 (1960).
[31] A. H. Morrish, in *Canted Antiferromagnetism: Hematite* (World Scientific, Singapore, 1995), pp. 81–85.
[32] H. Le Gall, C. Leycuras, D. Minella, E. G. Rudashewsky, and V. S. Merkoulov, Phys. B+C **86–88**, 1223 (1977).
[33] G. S. Krinchik and V. E. Zubov, ZhETF Pis. Red. **20**, 307 (1974) [JETP Lett. **20**, 137 (1974)].
[34] G. S. Krinchik, A. P. Khrebtov, A. A. Askochenskii, and V. E. Zubov, ZhETF Pis. Red. **17**, 466 (1973) [JETP Lett. **17**, 335 (1973)].
[35] A. T. Karaev and B. Y. Sokolov, Tech. Phys. **48**, 651 (2003).
[36] Ö. Özdemir and D. J. Dunlop, J. Geophys. Res. Solid Earth **119**, 2582 (2014).
[37] Y. Yang, J. B. Yi, X. L. Huang, J. M. Xue, and J. Ding, IEEE Trans. Magn. **47**, 3340 (2011).
[38] B. Vallina, J. D. Rodriguez-Blanco, A. P. Brown, L. G. Benning, and J. A. Blanco, J. Nanoparticle Res. **16**, 2322 (2014).
[39] Ö. Özdemir and D. J. Dunlop, J. Geophys. Res. Solid Earth **110**, 1 (2005).
[40] I. Sunagawa and P. J. Flanders, Philos. Mag. **11**, 747 (1965).
[41] H. Porath and C. B. Raleigh, J. Appl. Phys. **38**, 2401 (1967).
[42] M. L. Paramês, J. Mariano, Z. Viskadourakis, N. Popovici, M. S. Rogalski, J. Giapintzakis, and O. Conde, Appl. Surf. Sci. **252**, 4610 (2006).
[43] R. F. Butler and S. K. Banerjee, J. Geophys. Res. **80**, 4049 (1975).
[44] S. Banerjee, Nat. Phys. Sci. **232**, 15 (1971).
[45] S. M. Suturin, V. V Fedorov, A. M. Korovin, G. A. Valkovskiy, S. G. Konnikov, M. Tabuchi, and N. S. Sokolov, J. Appl. Crystallogr. **46**, 874 (2013).